Half-and quarter-metals in rhombohedral trilayer graphene

https://doi.org/10.1038/s41586-021-03938-w

Received: 8 April 2021

Accepted: 20 August 2021

Published online: 1 September 2021



Check for updates

Haoxin Zhou^{1,6}, Tian Xie^{1,6}, Areg Ghazaryan², Tobias Holder³, James R. Ehrets¹, Eric M. Spanton¹, Takashi Taniguchi⁴, Kenji Watanabe⁵, Erez Berg¹, Maksym Serbyn¹ & Andrea F. Young^{1⊠}

Ferromagnetism is most common in transition metal compounds where electrons occupy highly localized d orbitals. However, ferromagnetic order may also arise in low-density two-dimensional electron systems¹⁻⁵. Here we show that gate-tuned van Hove singularities in rhombohedral trilayer graphene⁶ drive spontaneous ferromagnetic polarization of the electron system into one or more spin and valley flavours. Using capacitance and transport measurements, we observe a cascade of transitions tuned to the density and electronic displacement field between phases in which quantum oscillations have fourfold, twofold or onefold degeneracy, associated with a spin- and valley-degenerate normal metal, spin-polarized 'half-metal', and spin- and valley-polarized 'quarter-metal', respectively. For electron doping, the salient features of the data are well captured by a phenomenological Stoner model⁷ that includes valley-anisotropic interactions. For hole filling, we observe a richer phase diagram featuring a delicate interplay of broken symmetries and transitions in the Fermi surface topology. Finally, we introduce a moiré superlattice using a rotationally aligned hexagonal boron nitride substrate^{5,8}. Remarkably, we find that the isospin order is only weakly perturbed, with the moiré potential catalysing the formation of topologically nontrivial gapped states whenever itinerant half- or quarter-metal states occur at half- or quarter-superlattice band filling. Our results show that rhombohedral graphene is an ideal platform for well-controlled tests of many-body theory, and reveal magnetism in moiré materials^{4,5,9,10} to be fundamentally itinerant in nature.

In metals, electronic interaction effects become dominant when the potential energy arising from the Coulomb repulsion becomes larger than the kinetic energy the electrons inherit from the band dispersion. This condition is captured by the Stoner criterion⁷, $UD_{\rm F} > 1$, which links the strength of the Coulomb repulsion, U, and the single-particle density of electronic states at the Fermi energy, D_F. The Stoner criterion provides the qualitative basis for ferromagnetism in transition metals, where a partially filled narrow band arising from the highly localized d orbitals contributes a large density of states at the Fermi level. However, quantitative modelling of ferromagnetism in metals relies heavily on approximate treatments of exchange and correlation effects, which are typically difficult to directly benchmark to experiment. Model systems such as the two-dimensional electron gas offer a path forward, providing a well-controlled venue to benchmark many-body theory using both more elaborate numerical methods¹ and, ideally, precision experiments. In this regard, graphene-based van der Waals heterostructures present a new opportunity due to their exceptionally low disorder and well-known single-particle band structures, and a high degree of in situ control using electric and magnetic fields.

In this Article, we focus on rhombohedrally stacked graphene trilayers, characterized by 'ABC' stacking order where A, B and C refer to inequivalent relative placements of individual graphene layers within the multilayer crystal (Fig. 1a). All rhombohedral graphite multilayers feature van Hove singularities at or near the band edge⁶ where the density of states diverges, which are enhanced by a perpendicular electric displacement field (Fig. 1b, c). Low-density ferromagnetism was predicted theoretically for bilayers shortly after the experimental isolation of graphene¹¹, but signatures of correlation physics at finite density have been observed only recently in rhombohedral trilayers¹², tetralayers¹³ and multilayers¹⁴. Moreover, experiments on rhombohedral trilayer graphene aligned to hexagonal boron nitride (hBN)^{5,8,15} have shown the emergence of a flat electronic band hosting correlation-driven insulators appearing at integer filling of the moiré superlattice unit cell. However, a microscopic, unified picture of these disparate effects has remained elusive.

Phase diagram of rhombohedral trilayer graphene

We measure the inverse electronic compressibility $\kappa = \partial \mu / \partial n_e$ (here μ is the chemical potential and n_e is the charge carrier density) as a function of n_e and the applied electric displacement field, D. Figure 1d, e shows κ for B = 0 and the base temperature of our dilution refrigerator. At all values of D, κ has a maximum at charge neutrality, consistent with

Department of Physics, University of California, Santa Barbara, CA, USA, 2 Institute of Science and Technology, Klosterneuburg, Austria, 3 Department of Condensed Matter Physics, Weizmann Institute of Science, Rehovot, Israel. 4International Center for Materials Nanoarchitectonics, National Institute for Materials Science, Tsukuba, Japan. 5Research Center for Functional Materials, National Institute for Materials Science, Tsukuba, Japan, ⁶These authors contributed equally: Haoxin Zhou, Tian Xie, [⊠]e-mail; andrea@physics.ucsb.edu

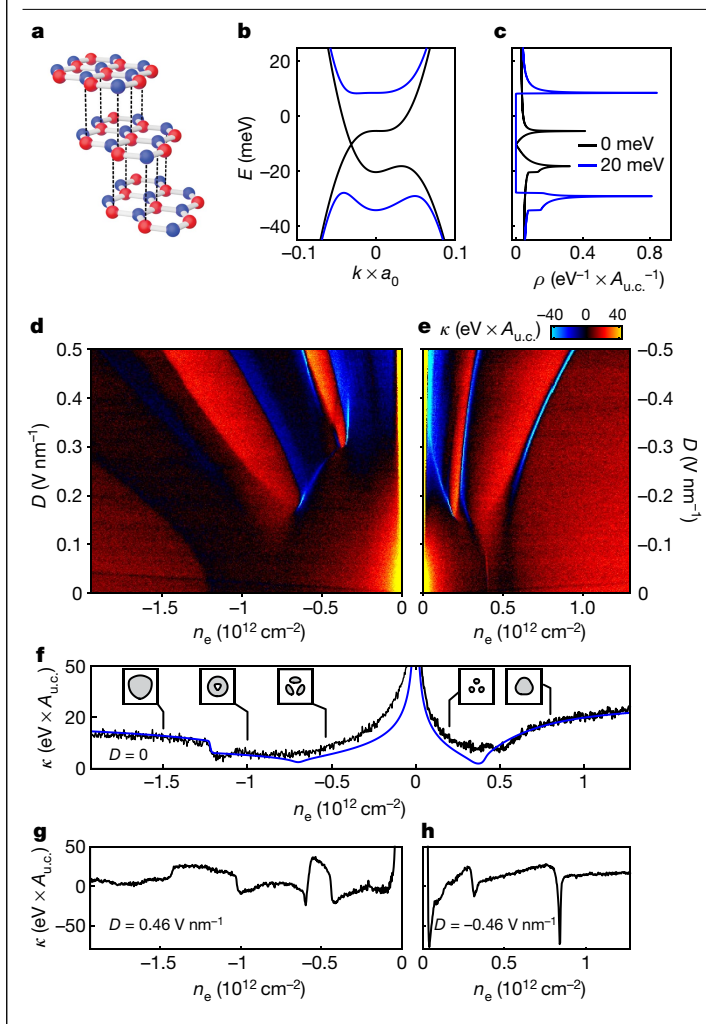


Fig. 1 | Spontaneous symmetry breaking in rhombohedral trilayer graphene. a, Crystal structure of rhombohedral trilayer graphene. b, Band structure of rhombohedral trilayer graphene with an interlayer potential $\Delta_1 = 0$ meV (black) and 30 meV (blue) calculated from the six-band continuum model (see Supplementary Information). Here $a_0 = 0.246$ nm is the graphene lattice constant. \mathbf{c} , Corresponding single-particle density of states, ρ , versus energy at zero temperature. d, e, False-colour plot of the inverse compressibility as a function of displacement field and carrier density for hole doping (d) and electron doping (e). f, Inverse compressibility measured at D=0(black) and inverse compressibility calculated from the single particle, six-band continuum model (blue). Insets: Fermi contours calculated from the continuum model (see also Supplementary Fig. 3). Contours are plotted as a function of wavevector near one of the corners of the Brillouin zone. The wavevector components k_x and k_y range between $-0.05a_0$ and $+0.05a_0$ in all plots. g, h, Inverse compressibility as a function of carrier density measured at $D = 0.46 \text{ V nm}^{-1}(\mathbf{g}) \text{ and } D = -0.46 \text{ V nm}^{-1}(\mathbf{h}).$

the Dirac nodes (for D=0) or displacement-field-induced bandgap (for |D|>0) expected from the single-particle band structure. At D=0, κ is marked by only two significant features at finite density in the form of a sharp step at $n_{\rm e}\approx -1.2\times 10^{12}{\rm cm}^{-2}$ and a kink at $n_{\rm e}\approx -1.2\times 10^{12}{\rm cm}^{-2}$. These features are qualitatively captured by the tight-binding band structure of Fig. 1b, c, and correspond to van Hove singularities arising from Lifshitz transitions in the Fermi sea topology, which is simply connected at high densities but is described by an annulus or multiple pockets at lower densities.

While some evidence of correlation-driven physics is evident for D=0 at $n_{\rm e}$ (Extended Data Fig. 2) and near $n_{\rm e}\approx 0.4\times 10^{12}{\rm cm}^{-2}$ (Extended Data Fig. 3), deviations from the single-particle picture are most evident at high |D|. The experimental κ features multiple regions of

near-constant compressibility separated by boundaries where κ is strongly negative—in contrast to the tight-binding model where large |D| simplifies the electronic structure (see Supplementary Information). Negative compressibility is generally associated with electronic correlations 16 , and may arise at first-order phase transitions characterized by phase separation. For electron doping, the high-|D| phase diagram appears to consist of three distinct phases at low, intermediate and high density separated by first-order phase transitions, while for hole doping ($n_{\rm e} < 0$) the phase diagram is more complex. In both cases, however, negative compressibility features develop at finite |D| and evolve towards higher $|n_{\rm e}|$ with increasing |D|. These features rapidly wash out as the temperature is raised, although associated features remain visible at 5 K (Extended Data Fig. 4).

The nature of competing phases is revealed by finite magnetic field measurements, shown for electron doping in Fig. 2a for a magnetic field $B_1 = 1$ T perpendicular to the sample plane. At this field, energy gaps between Landau levels are easily visible as peaks in the inverse compressibility, while the phase boundaries are only slightly altered relative to the B = 0 case. As is evident in Fig. 2a, the phase transitions observed at B = 0 separate regions of contrasting Landau level degeneracy. In the high-density phase, the Landau levels have the combined fourfold degeneracy of the spin and valley flavours native to graphene systems; similarly, at low n_e and low D, a 12-fold symmetry emerges due to additional degeneracy of local minima in the strongly trigonally warped Fermi surface^{17,18}. However, in the intermediate- and low-density phases, respectively, the degeneracy is reduced to twofold and one fold. This trend is evident in low-magnetic-field magnetoresistance oscillations in the three regimes, Fourier transforms of which are shown in Fig. 2b (see also Extended Data Fig. 5a-c and Extended Data Fig. 6). The loss of degeneracy is consistent with a zero-magnetic-field phase diagram that contains two distinct phases that spontaneously break the combined spin and valley isospin symmetry. In this picture, the intermediate-density phase consists of two degenerate Fermi surfaces at $B_1 = 0$, constituting a 'half-metal', compared to the normally fourfold degenerate graphene, while the low-density phase has a single Fermi surface and is thus a 'quarter-metal'.

Stoner ferromagnetism

To better understand the mechanisms leading to the rich magnetic phase diagram observed, we study a four-component Stoner model that includes both SU(4) symmetric interactions as well as a flavour-anisotropic Hund's coupling that favours the half-metal at the expense of the quarter-metal and an unphysical 'three-quarter-metal' state that otherwise arises in this model (see Methods and Supplementary Information). Calculated κ (Fig. 2c) shows a cascade of symmetry-broken phases with reduced Fermi surface degeneracy (Fig. 2d (inset) and Supplementary Information) following trajectories in the n_e -D plane very similar to those observed experimentally. This dependence can be directly related to the evolution of the band-edge van Hove singularities, which cause the Stoner criterion for ferromagnetism to be satisfied at ever higher $|n_e|$ with increasing |D| as more states accumulate near the band edge.

To constrain the precise broken symmetries in the half- and quarter-metal phases, we study the evolution of the phase transitions in an in-plane magnetic field, which couples primarily to the electron spin through the Zeeman effect. The resulting change in density at which a given transition occurs is directly proportional to the difference in Zeeman energy between the two competing phases, providing a sensitive probe of relative spin polarization. As shown in Fig. 2e, Zeeman energy favours the half-metal over the fully symmetric—and necessarily spin-unpolarized—state. Moreover, the phase transition density shows a cusp at B_{\parallel} implying an energy difference that is linear in B_{\parallel} as expected for a ferromagnetic half-metal with a divergent spin susceptibility at B=0. In contrast, the transition between half- and

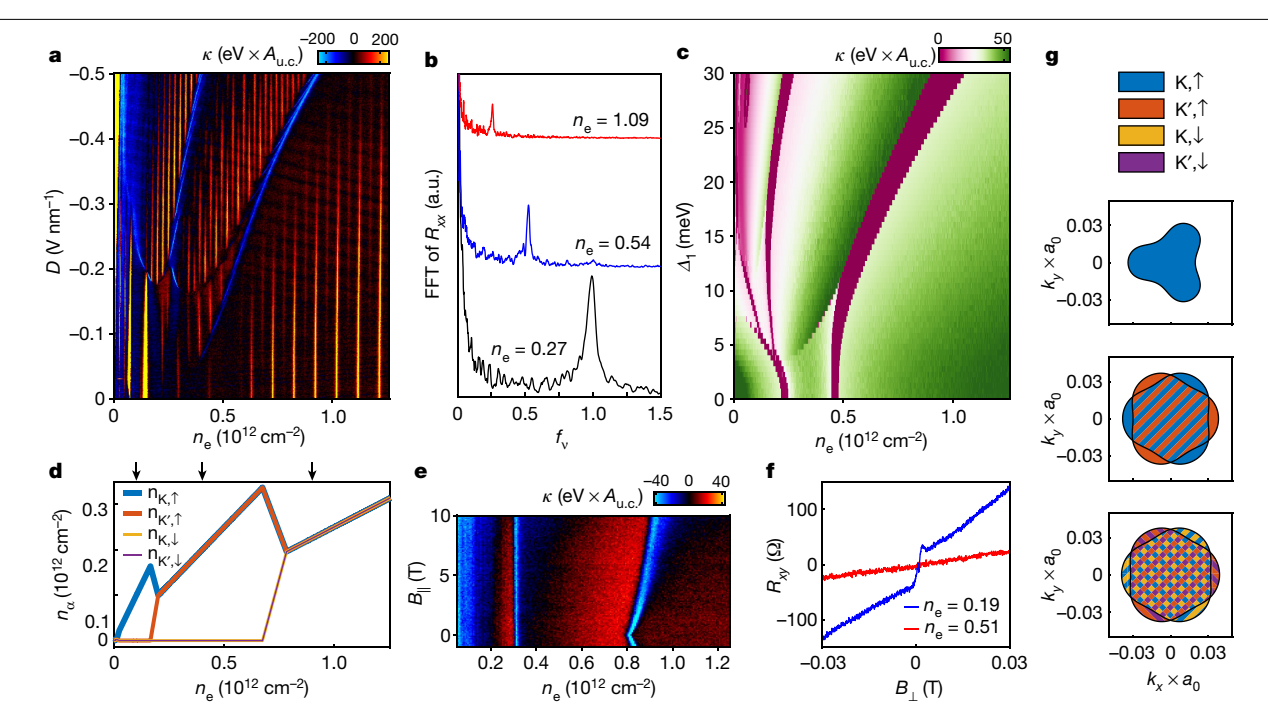


Fig. 2 | Stoner ferromagnetism in the conduction band. a, False-colour plot of the inverse compressibility κ measured at $B_1 = 1$ T. **b**, Fast Fourier transform (FFT) of $R_{xx}(1/B_1)$ at D = -0.43 V nm⁻¹ and the indicated values of n_{ex} expressed in units of 10^{12} cm⁻². Data are plotted as a function of $f_v = f_B/(\phi_0 n_e)$, where f_B is the oscillation frequency (measured in tesla) and $\phi_0 = h/e$ is the magnetic flux quantum. f_{y} can be interpreted as the fraction of the total Fermi surface area enclosed by a given orbit. \mathbf{c} , Inverse compressibility at B = 0 calculated from the Stoner model described in the main text with U = 30 eV, J = -9 eV. **d**, Partial

densities of each spin-valley flavour density calculated from the Stoner model at a fixed interlayer potential of 20 meV for the parameters in c. e, In-plane magnetic field dependence of the κ measured at $D = -0.43 \text{ V nm}^{-1}$. **f**, Hall resistivity, R_{xy} , measured at $n_e = 0.19 \times 10^{12} \text{cm}^{-2}$ (blue) and $n_e = 0.51 \times 10^{12} \text{cm}^{-2}$ (red). Both curves are measured at $D = -0.4 \text{ V nm}^{-1}$ and T = 0.5 K. g. Calculated Fermi contours of each flavour corresponding to the three carrier density values indicated by the arrows in d. The Fermi contours are colour coded to distinguish spin and valley flavours.

quarter-metal is unaffected by B_{\parallel} , consistent with identical, and presumably complete, spin polarization in both phases. Measurements of the Hall effect (Fig. 2f and Extended Data Fig. 8) show an anomalous Hall effect in the quarter-metal phase but no corresponding effect in the half-metal. This is expected due to the contrasting Berry curvatures in the two valleys, which cancel for valley-unpolarized states but may give rise to an intrinsic anomalous Hall effect for valley-polarized states²⁰. Taking these findings together, we conclude that the quarter-metal is spin and valley polarized while the half-metal is spin polarized but valley unpolarized (Fig. 2g). Interestingly, our results imply a ferromagnetic Hund's coupling (J < 0), in contrast to the quantum Hall ferromagnet in monolayer and bilayer graphene²¹.

Ferromagnetism in the valence band

Compared with the electron-doped case, hole-doped rhombohedral trilayer graphene shows a considerably more complex phase diagram, as seen in the $B_1 = 1$ T magnetocapacitance data shown in Fig. 3a. The contrast between the phase diagrams of the valence and conduction bands can be related to the single-particle band structure, which differs markedly between the two. Most importantly, in the valence band, the density of states diverges at a finite density $n_e \approx -0.5 \times 10^{12} \text{ cm}^{-2}$, which corresponds to the merger of three disjoint Fermi pockets at low hole density into a single annular Fermi surface. At still higher $|n_e|$, the small electron pocket centred at each corner of the Brillouin zone disappears, leading to a step discontinuity (Fig. 3b). As a result, density-driven phase transitions in the valence band may be of several general types. First, as in the conduction band, isospin symmetries may break, reducing the degeneracy of the Fermi surface. In addition, Lifshitz transitions in the topology of the Fermi surface, which are already evident in the single-particle band structure, may occur. Finally, the nonmonotonic

dependence of density of states on n_e may favour states with partial isospin polarization, analogous to conventional ferromagnets, and allowing for Lifshitz transitions of a second type in which new Fermi surfaces are nucleated in previously unoccupied spin/valley flavours. Empirically, we find that, compared to electron doping, some hole-doping transitions are more strongly first order, showing hysteresis as a function of both magnetic field (Fig. 3c) and gate voltage (Fig. 3d, e).

To disentangle these phases experimentally, we measure the resistivity as a function of perpendicular magnetic field and n_e and plot the Fourier transform of $R_{xx}(1/B_1)$ (Fig. 3f, g and Extended Data Fig. 5d, e) with frequencies normalized to that corresponding to the total carrier density. Peak position thus indicates the fractional share of the total electrons enclosed by a given Fermi contour. At the highest values of $|n_e|$, a single peak (and its harmonics) is visible at $f_e = 0.25$, consistent with four Fermi surfaces each enclosing an equal share of the total density. As n_e crosses the threshold of $n_e \approx -1.7 \times 10^{12} \text{cm}^{-2}$ in Fig. 3f (corresponding to the step in compressibility highlighted in Fig. 1d, e), the frequency of the quarter-density peak begins to grow, and a second peak emerges at low frequency. We interpret this as indicating a Lifshitz transition where a small electron Fermi surface is nucleated in the middle of the (now annular) Fermi sea, precisely as predicted by the single-particle band structure.

On further lowering of $|n_e|$ towards zero, a sudden transition in the quantum oscillations is observed near $n_e \approx -1.15 \times 10^{12} \text{cm}^{-2}$ in Fig. 3f. This threshold corresponds to a subtle but visible low- κ feature in Fig. 1g. On the low- n_e side of the transition, the oscillation frequencies are less well defined, but show spectral weight concentrated most prominently at f_w slightly less than 0.5 and at very low frequencies. These features are consistent with a Stoner-type transition to a partially isospin polarized (PIP) phase, with majority and minority charge carriers in two distinct pairs of isospin flavours. These contours

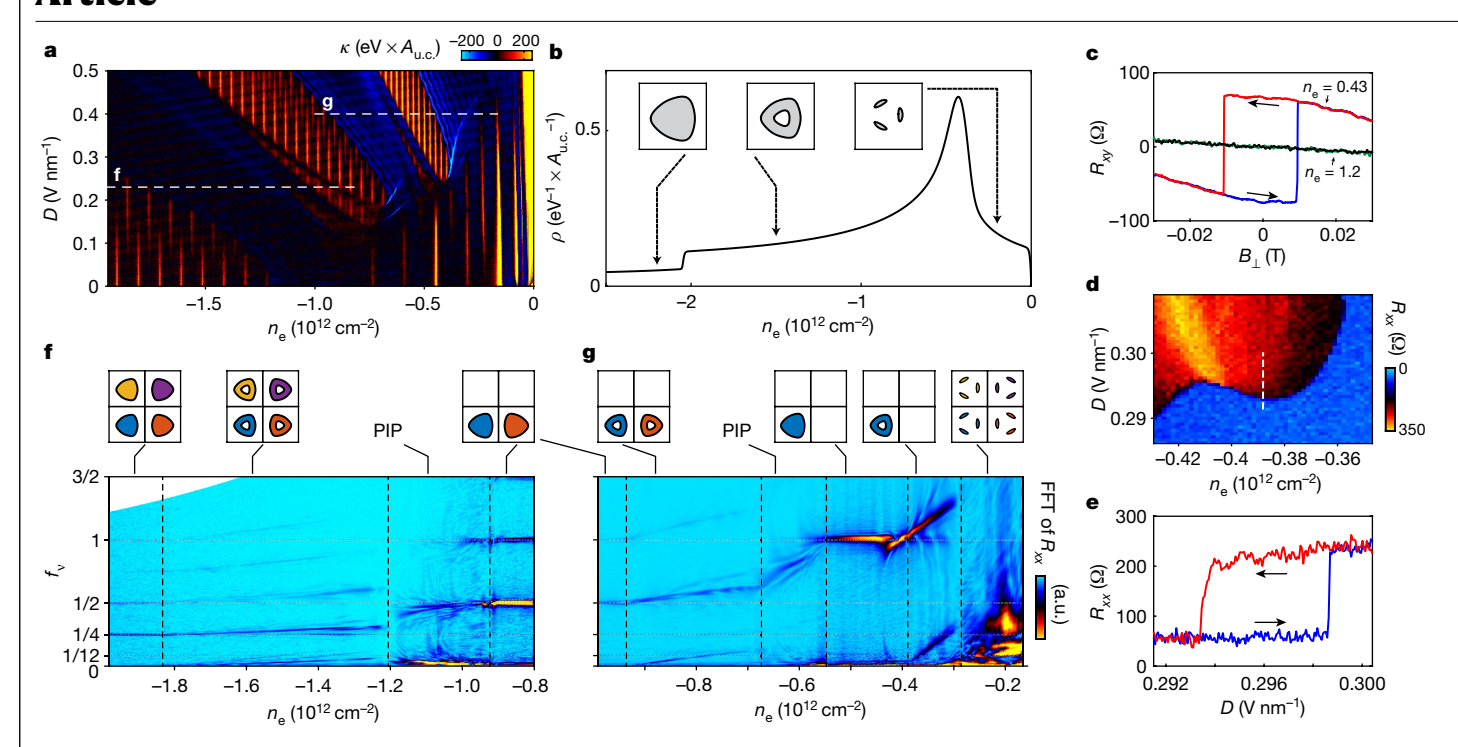


Fig. 3 | **Ferromagnetism and Fermi surface topology in the valence band. a**, κ measured at $B_{\perp} = 1$ T in the valence band. **b**, Density of states as a function of carrier density in the valence band for $\Delta_1 = 20$ meV calculated from the continuum model for a single isospin flavour. Insets: calculated Fermi contours at the indicated values of n_e , plotted on the interval $(-0.05a_0^{-1}, 0.05a_0^{-1})$ for both k_x and k_y , **c**, Low-magnetic-field Hall resistivity measured at D = 0.43 V nm⁻¹ at two values of n_e . A hysteretic anomalous Hall effect is observed in the valley-polarized quarter-metal, but not in the valley-unpolarized half-metal. **d**, Detail of the phase boundary between the quarter-metal and symmetric

low-density state measured at B=0. **e**, Resistivity measured as a function of D across this boundary at B=0. The transition is strongly first order, showing hysteresis as a function of applied gate voltages. **f**, Fourier transform of quantum oscillations in resistivity measured at D=0.23 V nm⁻¹ along the dashed line labelled 'f' in panel **a** (see Methods). The top panels show schematic depictions of Fermi contours in density domains distinguished by their quantum oscillations. **g**, As in **f**, but for D=0.4 V nm⁻¹, measured along the dashed line labelled 'g' in panel **a**.

continuously evolve until the $f_{\rm v}$ of the high-frequency peak converges to 0.5, whereupon the low-frequency peak disappears, consistent with a Lifshitz transition from the PIP phase into a half-metal. Remarkably, this pattern repeats itself as the density is lowered further, as shown in Fig. 3d: the simple half-metal transitions into a half-metal with an annular Fermi sea, then to a PIP phase with one majority and one minority flavour, then into a simple quarter-metal and then into an annular quarter-metal before isospin symmetry is restored at the lowest densities. At these very low densities, each isospin flavour hosts three Fermi pockets, leading to observed oscillation frequencies near $f_{\rm v}=1/12$.

As for the electron side, many of these transitions show a characteristic B_{\parallel} dependence (Extended Data Fig. 7) and an anomalous Hall effect (Extended Data Fig. 8) that allow us to confirm the spin and valley polarizations of the half- and quarter-metal states, which we find to be similar to those on the electron side. We note, however, that transitions do not generally show simple linear-in- B_{\parallel} behaviour. In addition, the complexity of the finite B_{\perp} magnetoresistance suggests that these domains may harbour multiple PIP phases.

Effect of a moiré potential

Experimental indications of strong interactions in intrinsic rhombohedral graphene have previously been restricted to the very low-density ($|n_{\rm e}| < 10^{11} {\rm cm}^{-2}$) regime^{12,14}. Recently, however, manifestations of strong interaction have emerged in rhombohedral trilayers aligned to hBN at densities comparable to the phase transitions reported here^{5,8,15}. In these devices, insulating states have been observed at filling $\nu=-1$ and -2 of the superlattice unit cell, including an incipient Chern insulator at $\nu=-1$. These experimental findings were interpreted in terms of

a moiré-induced flat band. It is interesting to reexamine this picture in light of our finding that rhombohedral trilayers spontaneously break symmetries.

Comparing κ for a moiré device (Fig. 4a) with that for a non-moiré device in Figs. 1–3, we find that κ features associated with Stoner transitions are only weakly affected by the superlattice potential. The primary difference is the appearance of incompressible states at commensurate fillings $v=\pm 1$, ± 2 of the moiré unit cell. The relationship between these insulators and the underlying symmetry breaking in non-moiré devices is depicted schematically in Fig. 4b, where we overlay the phase boundaries measured in intrinsic trilayers with the domain of stability of the commensurate, incompressible states in moiré-patterned trilayers. Evidently, incompressible states emerge whenever the superlattice filling is divisible by the degeneracy of the Fermi surface in the non-moiré system at the same $n_{\rm e}$ and D. The effect of the moiré can thus be understood as a perturbation that does not qualitatively alter the correlated electron physics already present in the parent trilayer.

We observe several classes of commensurate gapped states driven by electron interaction in the moiré sample. Consistent with prior work, we find that commensurate insulators at v = -1 and v = -2 are topologically trivial for D > 0 while the v = -1 insulator is nontrivial for D < 0 (Fig. 4c), hosting a competition between Chern insulators with Chern number C = -2 and C = -3 (see Methods). We also observe a number of features at fractional filling of the moiré superlattice bands (Fig. 4d). These states are all found to have zero Chern number in the low- B_{\perp} limit and occur at v = 1/3, 1/2, 2/3... The regime where these states are observed corresponds within single-particle band structure models to a regime where an unusually flat topologically trivial flat band is partially filled²². We interpret them as

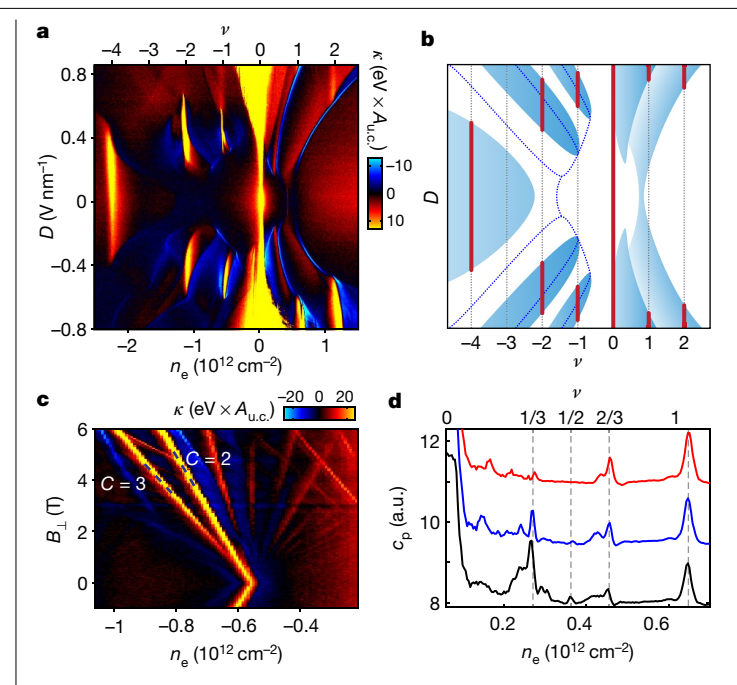


Fig. 4 | Effect of a moiré superlattice potential. a, κ measured in sample B where the lattice of the rhombohedral trilayer graphene is aligned to that of one of the encapsulating hBN crystals. b, Schematic illustration of the formation of insulating states. Dotted lines indicate Lifshitz transitions described in Fig. 3 and blue regions indicate domains of half- and quarter-metal states in the absence of the moiré potential. Red lines represent the insulating states observed in the moiré superlattice sample, which occur whenever the moiré filling is divisible by the degeneracy of the underlying metal. c, κ in sample B measured at $D = -0.56 \text{ V nm}^{-1}$ as a function of n_e and $B_1 \cdot \mathbf{d}$, Penetration field capacitance data as a function of n_e at $D = -0.82 \text{ V nm}^{-1}$ (black), -0.86 V nm^{-1} (blue) and -0.89 V nm⁻¹ (red). The curves are offset for clarity. Filling factors of some incompressible states are marked on the top axis.

generalized Wigner crystals, in which electron repulsion leads to commensurate filling of the moiré potential, breaking the superlattice symmetry^{23,24}.

Discussion

It is interesting to compare the itinerant ferromagnetism revealed in rhombohedral trilaver graphene with other physical realizations of ferromagnetism. Unlike in transition metals, ferromagnetism in trilayer $graphene\,does\,not\,originate\,from\,tightly\,localized\,atomic\,orbitals, but$ rather is intrinsic to the itinerant electrons themselves. Rhombohedral trilayer graphene may also be contrasted with low-density semiconductors^{2,3}. While superficially similar, signatures of ferromagnetism in these systems are observed in an insulating regime, where electron wavefunctions are localized either by disorder or Wigner crystallization.

Despite the lack of an applied magnetic field, the underlying physics of rhombohedral trilayer graphene closely resembles that of a quantum Hall ferromagnet. Indeed, the sharp peak in the density of states associated with the van Hove singularity plays a similar role to that of a Landau level: high density of states allows a large gain of exchange energy by isospin polarization, at a small cost in kinetic energy. As in a Landau level, the electronic wavefunctions corresponding to the region where the density of states is high are strongly overlapping, enhancing the exchange coupling.

These considerations apply equally well to isospin magnetism in moiré heterostructures, which is thought to underpin the correlated physics observed in these systems²⁵. From this point of view, it is the high density of states of the flat bands, and not their isolation from high-energy dispersive bands, that plays the central role in the ferromagnetic order. As demonstrated here, the primary role of the moiré potential is to enable gapped states at finite density. In this light, our results suggest a new design space for van der Waals heterostructures, based on gate-tunable isospin magnetism as a building block that is both strongly correlated but also well understood.

Online content

Any methods, additional references. Nature Research reporting summaries, source data, extended data, supplementary information, acknowledgements, peer review information; details of author contributions and competing interests; and statements of data and code availability are available at https://doi.org/10.1038/s41586-021-03938-w.

- Tanatar, B. & Ceperley, D. M. Ground state of the two-dimensional electron gas, Phys. Rev. B 39, 5005-5016 (1989)
- 2. Pudalov, V. M., Kuntsevich, A. Y., Burmistrov, I. S. & Reznikov, M. Thermodynamic studies of two-dimensional correlated electron systems. J. Low Temp. Phys. 181, 99-111 (2015).
- Hossain, M. S. et al. Observation of spontaneous ferromagnetism in a two-dimensional electron system. Proc. Natl Acad. Sci. USA 117, 32244-32250 (2020).
- Sharpe, A. L. et al. Emergent ferromagnetism near three-quarters filling in twisted bilayer graphene, Science 365, 605-608 (2019)
- Chen, G. et al. Tunable correlated Chern insulator and ferromagnetism in a moiré superlattice, Nature 579, 56-61 (2020).
- Zhang, F., Sahu, B., Min, H. & MacDonald, A. H. Band structure of ABC-stacked graphene trilavers, Phys. Rev. B 82, 035409 (2010).
- Stoner, E. C. Collective electron ferromagnetism. Proc. R. Soc. A 165, 372-414 (1938).
- Chen, G. et al. Evidence of a gate-tunable Mott insulator in a trilayer graphene moiré 8 superlattice, Nat. Phys. 15, 237-241 (2019).
- 9. Serlin, M. et al. Intrinsic quantized anomalous Hall effect in a moiré heterostructure. Science 367, 900-903 (2020).
- 10 Polshyn, H. et al. Electrical switching of magnetic order in an orbital Chern insulator. Nature 588, 66-70 (2020).
- 11 Castro, E. V., Peres, N. M. R., Stauber, T. & Silva, N. A. P. Low-density ferromagnetism in biased bilayer graphene. Phys. Rev. Lett. 100, 186803 (2008).
- Lee, Y. et al. Gate tunable magnetism and giant magnetoresistance in ABC-stacked few-layer graphene. Preprint at https://arxiv.org/abs/1911.04450 (2019).
- Kerelsky, A. et al. Moiréless correlations in ABCA graphene, Proc. Natl Acad. Sci. USA 118 4 (2021).
- 14. Shi, Y. et al. Electronic phase separation in multilayer rhombohedral graphite. Nature 584, 210-214 (2020).
- 15. Chen, G. et al. Signatures of tunable superconductivity in a trilayer graphene moiré superlattice. *Nature* **572**, 215–219 (2019).
- Eisenstein, J. P., Pfeiffer, L. N. & West, K. W. Negative compressibility of interacting two-dimensional electron and quasiparticle gases. Phys. Rev. Lett. 68, 674-677 (1992).
- Varlet, A. et al. Anomalous sequence of quantum Hall liquids revealing a tunable Lifshitz transition in bilayer graphene. Phys. Rev. Lett. 113, 116602 (2014).
- Zibrov, A. A. et al. Emergent Dirac gullies and gully-symmetry-breaking quantum Hall states in ABA trilayer graphene. Phys. Rev. Lett. 121, 167601 (2018).
- Zondiner, U. et al. Cascade of phase transitions and Dirac revivals in magic-angle graphene, Nature 582, 203-208 (2020).
- Xiao, D., Chang, M.-C. & Niu, Q. Berry phase effects on electronic properties. Rev. Mod. Phys. 82, 1959-2007 (2010).
- Dean, C., Kim, P., Li, J. I. A. & Young, A. F. in Fractional Quantum Hall Effects: New Developments (eds Halperin, B. I. & Jain, J. K.) 317-375 (World Scientific, 2020).
- Zhang, Y.-H., Mao, D., Cao, Y., Jarillo-Herrero, P. & Senthil, T. Nearly flat Chern bands in moiré superlattices, Phys. Rev. B 99, 075127 (2019).
- Regan, E. C. et al. Mott and generalized Wigner crystal states in WSe₂/WS₂ moiré superlattices. Nature 579, 359-363 (2020).
- $\hbox{Xu, Y. et al. Correlated insulating states at fractional fillings of moir\'e superlattices.} \textit{Nature}$ 587, 214-218 (2020).
- Balents, L., Dean, C. R., Efetov, D. K. & Young, A. F. Superconductivity and strong correlations in moiré flat bands. Nat. Phys. 16, 725-733 (2020).

Publisher's note Springer Nature remains neutral with regard to jurisdictional claims in published maps and institutional affiliations.

© The Author(s), under exclusive licence to Springer Nature Limited 2021

Methods

The trilayer graphene and hBN flakes were prepared by mechanical exfoliation of bulk crystals. The rhombohedral domains of trilayer graphene flakes were detected by a Horiba T64000 Raman spectrometer with a 488-nm mixed-gas Ar/Kr ion laser beam. The rhombohedral domains were subsequently isolated using a Dimension Icon 3100 atomic force microscope 26,27 . The Van der Waals heterostructures were fabricated following a dry transfer procedure 28 . A special stacking order was followed to minimize the mechanical stretching of rhombohedral trilayer graphene. The details are described in Extended Data Fig. 1. We use dual-graphite-gated devices 29 , which minimize the charge disorder, enabling us to probe the intrinsic properties of these structures as a function of both carrier density, $n_{\rm e}$, and the applied perpendicular electric displacement field, D (see Supplementary Fig. 1).

All electronic measurements were performed in dilution refrigerators equipped with a superconducting magnet. To probe the ground-state thermodynamic properties of rhombohedral trilayers, we measure the penetration field capacitance 16 , which is directly proportional to the inverse electronic compressibility $\kappa = \partial \mu/\partial n_{\rm e}$ (where μ is the chemical potential and $n_{\rm e}$ is the charge carrier density). Capacitance data for the unaligned sample A are largely symmetric under $D \rightarrow -D$; however, for $n_{\rm e} \times D > 0$, a high-resistance single-gated region is introduced to the contact area where only one of the gates acts on the channel. We thus focus on the $n_{\rm e} \times D < 0$ quadrants in the bulk of our analysis, with data over the dull $n_{\rm e}$, D range shown in Extended Data Fig. 10.

Penetration field capacitance was measured using a capacitance bridge circuit with an FHX15X high-electron-mobility transistor serving as an in situ impedance transformer²⁸. An excitation frequency of 10,245.12 Hz was used to obtain the data in Fig. 4d. The rest of the $capacitance\,data\,were\,measured\,at\,54,\!245.12\,Hz.\,The\,quantity\,directly$ measured is $M = \frac{c_p + c_{parasitic}}{c_{cos}}$, where c_p is the capacitance between the top and bottom gate, c_{ref} is the capacitance of the reference capacitor and $c_{\text{parasitic}}$ is the parasitic capacitance of the instrument. The inverse compressibility is related to c_p by $c_p = \frac{c_1 c_b}{c_1 + c_b + \kappa^{-1}} \approx \kappa c_t c_b$ (ref. ²⁸), where $c_{\text{t(b)}}$ is the geometric capacitance between the top (bottom) gate and the trilayer graphene. To obtain κ , M is measured at two extremes, denoted M_{∞} and M_0 . M_{∞} corresponds to when the trilayer graphene is a good metal and is achieved by applying a large out-of-plane magnetic field and tuning the Fermi level within a partially filled Landau level. M_0 corresponds to when the trilayer is incompressible, which can be achieved by applying a large displacement field, D, while keeping the carrier density $n_e = 0$. In the former case $c_p = 0$; therefore, $M_{\infty} = c_{\text{parasitic}}/c_{\text{ref}}$. In the latter case, $c_{\text{p}} = (M_0 - M_{\infty})c_{\text{ref}} = \frac{c_1 c_b}{c_1 + c_b}$. From the equations above, $\kappa = \frac{1}{2c} \frac{M - M_{\infty}}{M_0 - M_{\infty}}$, where the averaged geometric capacitance $c_{\text{p}} = \frac{c_1 c_b}{c_1 + c_b}$ and $c_{\text{p}} = \frac{c_1 c_b}{c_1 + c_b}$. tance $c = \frac{c_t + c_b}{2}$ can be obtained by linear fitting of the carrier density, n_e , which is known for fixed Landau level filling providing a calibration standard.

Transport measurement was performed using a lock-in amplifier. The frequency was chosen between 17.777 Hz and 42.5 Hz to minimize the noise. A series of cryogenic high-pass filters were applied to reduce the electron temperature.

To analyse the magnetoresistance oscillations, a fifth-order polynomial fit is subtracted from the $R_{xx}\left(\frac{1}{B_\perp}\right)$ data. The data are then interpolated to produce an even grid as a function of $1/B_\perp$. Fourier transforms are computed over a range of $B_\perp \in (0.02 \text{ T}, 0.33 \text{ T})$ for Fig. 2b, (0.3 T, 1 T) for Fig. 3c and (0.02 T, 1 T) for Fig. 3d. The lower bound of B_\perp is chosen by the lowest B_\perp where oscillations are visible, and the upper bound is chosen to avoid obvious B_\perp -induced phase transitions. Raw magnetoresistance data for the Fourier transforms shown in the main text are presented in Extended Data Fig. 5.

The Stoner model used to generate Fig. 2c, d is based on a grand potential (per unit area) of the form:

$$\frac{\Phi}{A} = \sum_{\alpha} E_0(\mu_{\alpha}) + \frac{UA_{\text{u.c.}}}{2} \sum_{\alpha \neq \beta} n_{\alpha} n_{\beta} + \mu \sum_{\alpha} n_{\alpha}.$$

Here A and $A_{\rm u.c.}$ are the area of the sample and unit cell, respectively, α and β index the four spin and valley flavours, and n_{α} and μ_{α} are the density and chemical potential for a given flavour α . The first term, with $E_0(\mu_{\alpha}) = \int_0^\mu \epsilon \rho(\epsilon) d\epsilon$, where $\rho(\epsilon)$ is a density of states per area, accounts for the kinetic energy, and is minimized by occupying all flavours equally. The second term accounts for the effect of exchange interactions, whose strength is parameterized by a constant energy U and which we assume to be symmetric within the spin and valley isospin space. The exchange energy is minimized when fewer flavours are occupied.

As written, this model deviates significantly from the experimental data, predicting a threefold degenerate phase that is not observed. The spurious phase is also present in microscopic Hartree-Fock calculations (Supplementary Information), and can be traced to the artificial SU(4) symmetry of interactions within these models. More accurately, the internal symmetry group of rhombohedral trilayer graphene consists of SU(2) spin conservation, charge conservation, time reversal and the lattice symmetries. Within this lower-symmetry group, a variety of interactions that are anisotropic within the spin and valley space are allowed, particularly Hund's-type couplings that favour phases with particular broken spin and/or valley symmetries (see Supplementary Information). This problem has been considered in the context of spontaneous symmetry breaking in graphene quantum Hall ferromagnets^{30,31}, taking the form of an intervalley spin exchange coupling that favours the formation of a canted antiferromagnetic state at charge neutrality. Motivated by this observation, we introduce a flavour anisotropy of the form $\frac{\Phi'}{A} = JA_{\text{u.c.}}(n_{\text{K},\uparrow} - n_{\text{K},\downarrow})(n_{\text{K}',\uparrow} - n_{\text{K}',\downarrow})$. For J > 0, this term favours opposite spin polarizations in the two valleys, as is thought to occur in graphene quantum Hall ferromagnets, while for J<0 this term corresponds to a Hund's coupling and favours valley-unpolarized, spin ferromagnetic ground states. The phase diagram including this term—which is independent of the sign of *I*—is shown in Fig. 2c, d for U = 30 eV, with |I|/U = 0.3.

To analyse the incompressible states in the moiré sample, we measure the slopes of the incompressible states in the n_e - B_1 plane. In crystalline systems, incompressible gapped states can occur only at commensurate fillings of the lattice, and the moiré superlattice is qualitatively important in that it allows for gapped states at carrier densities that can be reached by electrostatics gates. Gapped states are classified by two quantum numbers, s and t, which respectively encode the number of electrons per lattice site and the Chern number, which is linked to the quantized Hall conductivity. We classify gaps by the resulting trajectories in the n- B_1 plane, $v = tn_{\phi} + s$, where n_{ϕ} is the number of magnetic flux quanta per unit cell. Consistent with the findings of prior work, our findings show that commensurate insulators at v = -1 and v = -2 due to the formation of a pnjunction nea D > 0, with s, t = (-1, 0) and (-2, 0), respectively (Extended Data Fig. 9). In contrast, the v = -1 insulator is nontrivial for D < 0 (Fig. 4c). Our high-resolution data allow us to observe a close competition between robust t = -2 and t = -3 Chern insulators for s = -1. At high magnetic field, these states occur at different densities, and high inverse compressibility peaks are observed corresponding to both trajectories. As B_1 tends to zero and the states converge to the same density, the t = -2 state wins the energetic competition, consistent with transport data⁵ (Extended Data Fig. 9).

Data availability

The data that support the findings of this study are available from the corresponding author on reasonable request.

- Masubuchi, S., Ono, M., Yoshida, K., Hirakawa, K. & Machida, T. Fabrication of graphene nanoribbon by local anodic oxidation lithography using atomic force microscope. *Appl. Phys. Lett.* 94 082107 (2009).
- Li, H. et al. Electrode-free anodic oxidation nanolithography of low-dimensional materials. Nano Lett. 18, 8011–8015 (2018).
- Wang, L. et al. One-dimensional electrical contact to a two-dimensional material. Science 342, 614–617 (2013).
- Zibrov, A. A. et al. Tunable interacting composite fermion phases in a half-filled bilayer-graphene Landau level. Nature 549, 360–364 (2017).
- Alicea, J. & Fisher, M. P. A. Interplay between lattice-scale physics and the quantum Hall effect in graphene. Solid State Commun. 143, 504–509 (2007).
- 31. Kharitonov, M. Phase diagram for the v = 0 quantum Hall state in monolayer graphene. Phys. Rev. B 85, 155439 (2012).
- Cong, C. et al. Raman characterization of ABA- and ABC-stacked trilayer graphene. ACS Nano 5, 8760–8768 (2011).
- Polshyn, H. et al. Quantitative transport measurements of fractional quantum Hall energy gaps in edgeless graphene devices. Phys. Rev. Lett. 121, 226801 (2018).

Acknowledgements We acknowledge discussions with A. MacDonald, L. Fu, F. Wang and M. Zaletel. A.F.Y. acknowledges support from the National Science Foundation under DMR-1654186, and the Gordon and Betty Moore Foundation under award GBMF9471. We acknowledge the use of the research facilities within the California NanoSystems Institute,

supported by the University of California, Santa Barbara and the University of California, Office of the President. K.W. and T.T. acknowledge support from the Elemental Strategy Initiative conducted by the MEXT, Japan (grant number JPMXP0112101001) and JSPS KAKENHI (grant numbers 19H05790 and JP20H00354). E.B. and T.H. were supported by the European Research Council under grant HQMAT (grant agreement number 817799). A.G. acknowledges support by the European Unions Horizon 2020 research and innovation programme under the Marie Sklodowska-Curie grant agreement number 754411.

Author contributions H.Z. and T.X. fabricated the device with assistance from E.M.S. and J.R.E. H.Z. performed the measurements, advised by A.F.Y. K.W. and T.T. grew the hBN crystals. A.G., T.H., E.B. and M.S. contributed to the theoretical interpretation and performed the numerical simulations. H.Z., A.G., M.S., E.B. and A.F.Y. wrote the manuscript with input from all authors.

Competing interests The authors declare no competing interests.

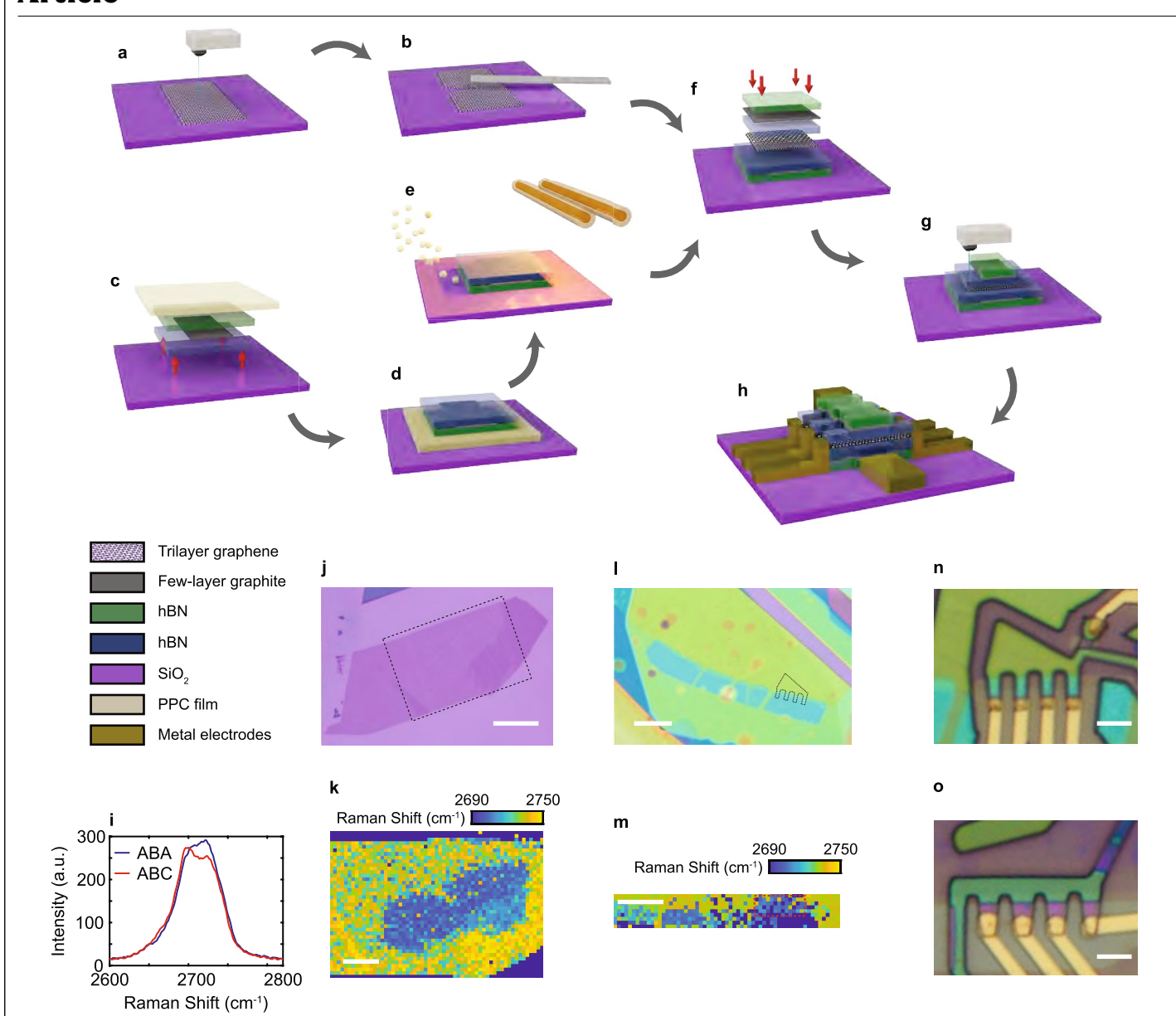
Additional information

 $\textbf{Supplementary information} \ The online version contains supplementary material available at \ https://doi.org/10.1038/s41586-021-03938-w.$

Correspondence and requests for materials should be addressed to Andrea F. Young.

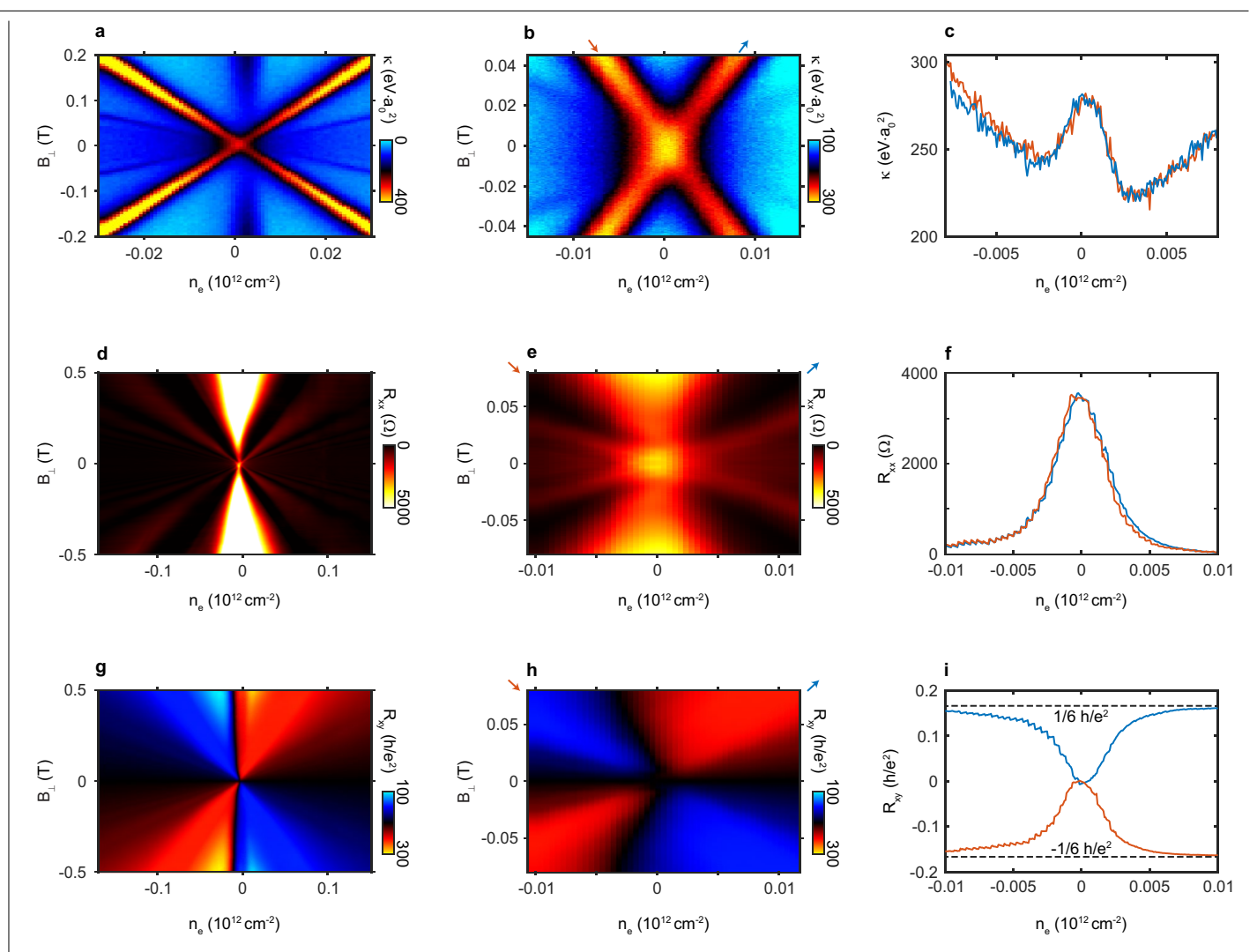
Peer review information Nature thanks Mikito Koshino and the other, anonymous, reviewer(s) for their contribution to the peer review of this work. Peer reviewer reports are available.

Reprints and permissions information is available at http://www.nature.com/reprints.



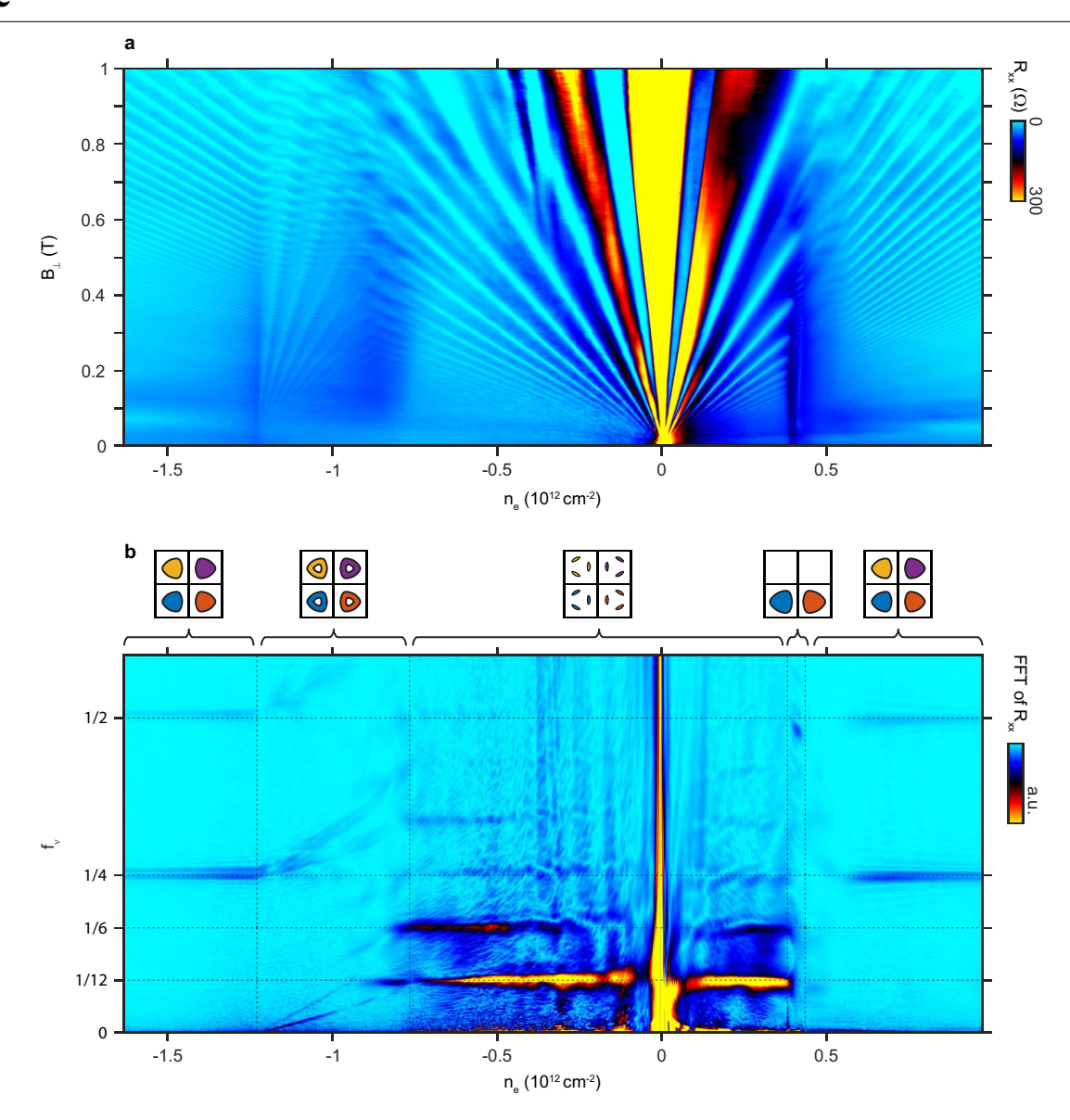
Extended Data Fig. 1 | **Sample fabrication procedure. a**, ABC-stacked domains in mechanically exfoliated trilayer graphene flakes are identified by taking the Raman spectra and extracting the peak maximum corresponding to the 2D mode 32 . **b**, ABC-stacked domains are isolated using atomic force microscope based anodic oxidation lithography 27 . **c**, The lower part of the heterostructure is assembled on a polypropylene carbonate (PPC) film which is then **d**, flipped as it is deposited onto the target substrate 33 . **e**, The sample is then vacuum annealed at 375 °C to remove the PPC film under the heterostructure. **f**, The upper part of the heterostructure, which contains the top graphite gate, trilayer graphene and hBN, is assembled separately and deposited onto the lower part of the heterostructure. **g**, The top hBN and top graphite gate are etched with XeF $_2$ followed by O $_2$ plasma to open windows on the heterostructure, allowing the stacking order to be confirmed after the manipulations of step f. **h**, The heterostructure is etched with CHF $_3$ and O $_2$ plasma and metal is deposited to form electrical contacts. **i**, Typical Raman

spectra of ABA- and ABC-stacked trilayer graphene, centered on the 2D mode. **j.** Optical micrograph of the trilayer graphene flake used to fabricate Sample A. Scale bar represents 20μm. **k**, Raman spectrum map of the trilayer graphene flake in panel j. The color represents the peak position of the 2D mode. The scan range is indicated in black dashed line in panel j. The scale bar represents 10μm. **l.** Optical micrograph of partially processed Sample A. The cyan regions are where the top graphite gate and the hBN on top of it has been etched. Since the bottom gate does not overlap with the etched window, this allows inspection with Raman spectroscopy of the stacking order of the trilayer graphene. The sale bar represents 10μm. The rough location of the actual device is indicated by black dashed line. **m**, Raman spectrum map of the partially processed Sample A. The region surrounded by a red boundary box remains in ABC-stacking order, which later became the active device region for sample A. **n**, Optical micrograph of Sample A after fabrication. Scale bar represents 3μm. **o**, Optical micrograph of Sample B. Scale bar represents 3μm.

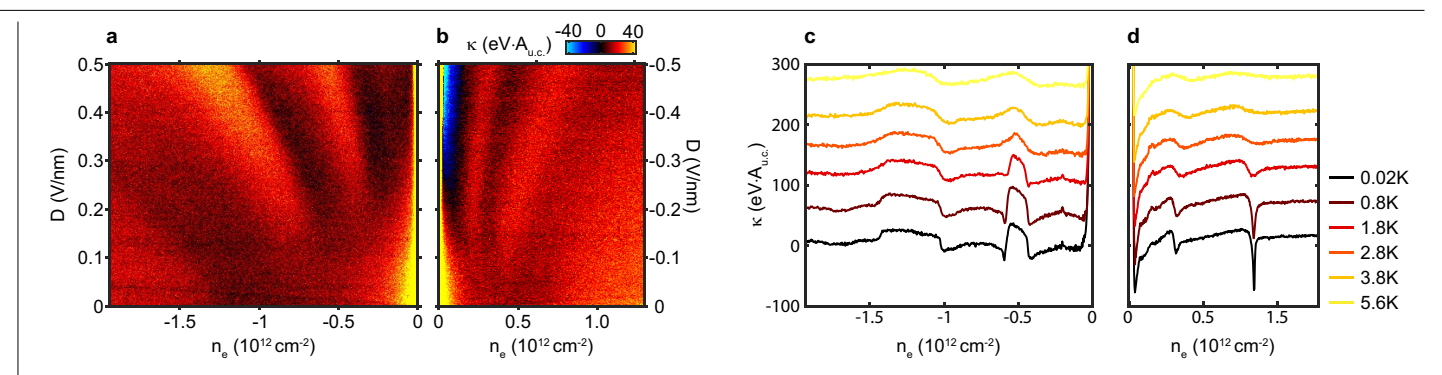


Extended Data Fig. 2 | **Measurements at low carrier density and displacement field. a**, Inverse compressibility versus carrier density and out-of-plane magnetic field near the charge neutrality point at D=0. **b**, Zoom-in of a. **c**, Line-cuts of b along the direction indicated by the arrows in b. **d**, R_{xx} versus carrier density and out-of-plane magnetic field near the

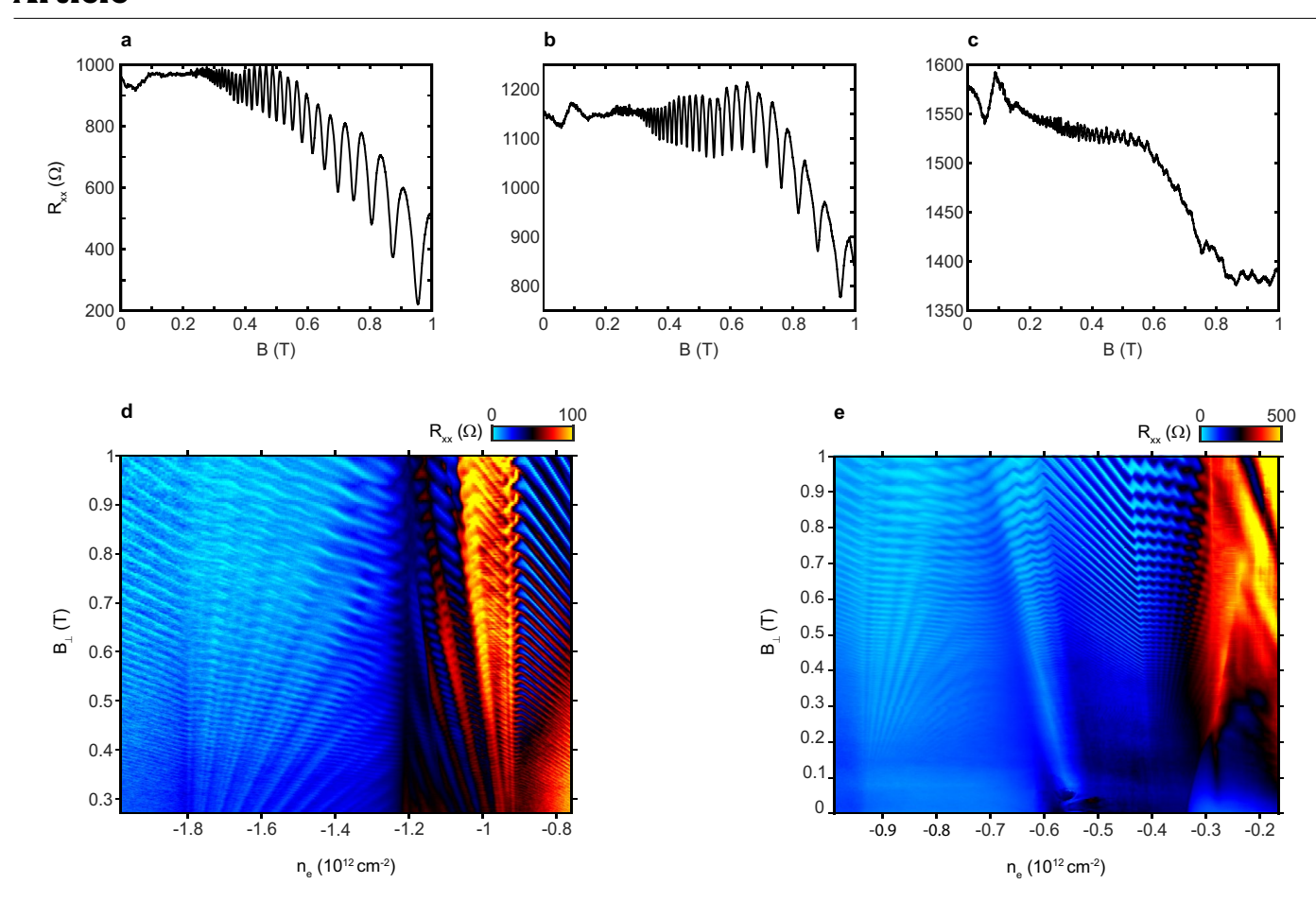
charge neutrality point at D=0. **e**, Zoom-in of d. **f**, Line-cuts of e along the direction indicated by the arrows in e. **g**, R_{xy} versus carrier density and out-of-plane magnetic field near the charge neutrality point at D=0. **h**, Zoom-in of g. **i**, Line-cuts of h along the direction indicated by the arrows in h.



Extended Data Fig. 3 | **Shubnikov de Haas oscillation at** D = 0 in **Sample A.** a, R_{xx} vs n_e and B_\perp measured at D = 0. **b**, Fast Fourier transform of data in **a**, the range of B_\perp chosen is 0.02T to 1T. The multiple phases are schematically represented by the Fermi contours on the top.

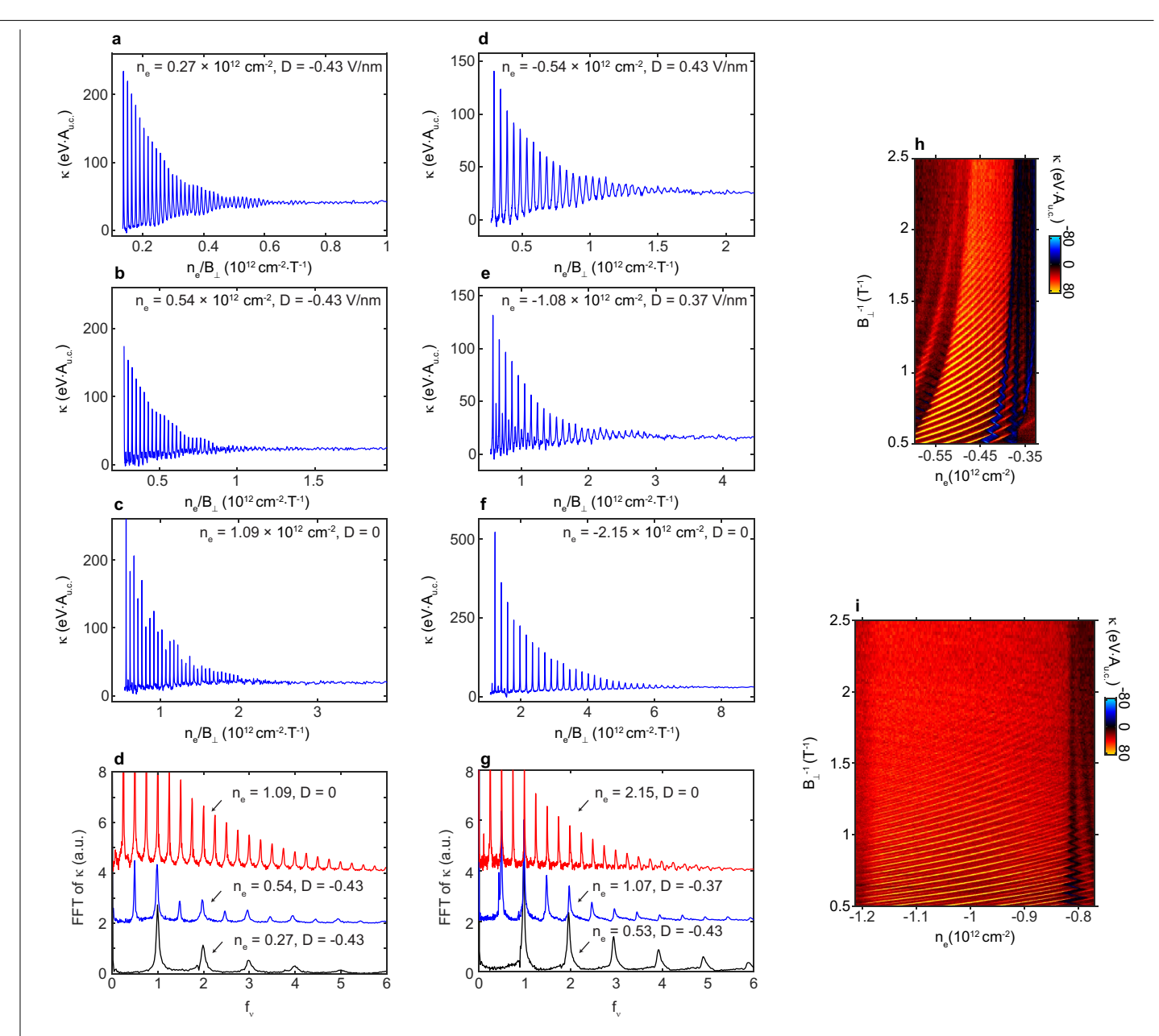


Extended Data Fig. 4 | **Shubnikov de Haas oscillation at** D = 0 **in Sample A. a**, b, Inverse compressibility as function of carrier density and displacement measured at T = 5.6K. **c**, **d**, Inverse compressibility as a function of carrier density measured at various temperatures at D = 0.46 V/nm (**c**) and -0.46 V/nm (**d**). Each curve is offset by 50eV·A_{u.c.} for clarity.



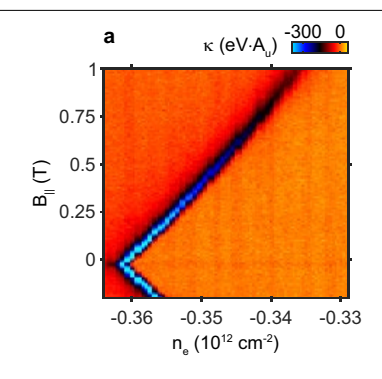
Extended Data Fig. 5 | **Shubnikov de Haas oscillations in Sample A. a, c,** R_{xx} vs B_{\perp} at electron doping. The measurements are performed at D=-0.43V/nm at $n_{\rm e}=0.27\times 10^{12}$ cm $^{-2}$ in **a,** 0.54×10^{12} cm $^{-2}$ in **b** and 1.09×10^{12} cm $^{-2}$ in **c.** The fast Fourier transform in Fig. 2b was calculated from these results. **d, e,** R_{xx} vs $n_{\rm e}$ and

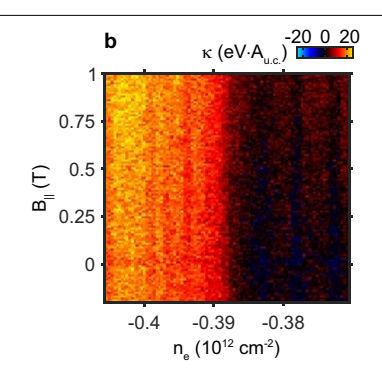
 $B_{\rm L}$ at hole doping. Data in panel **d** are measured at D=0.23 V/nm. Data in panel **e** are measured at D=0.4 V/nm. The fast Fourier transforms in Fig. 3c, d are calculated from these results.

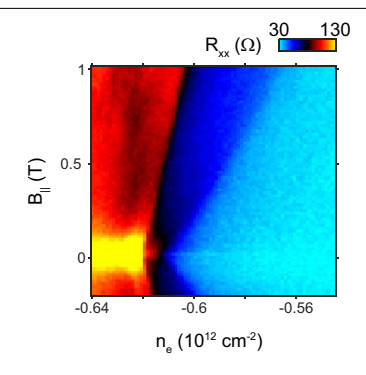


Extended Data Fig. 6 | Quantum capacitance magneto-oscillations. a-f, Inverse compressibility as a function of the out-of-plane magnetic field at fixed $n_{\rm e}$ and D. g, h, Inverse compressibility versus the out-of-plane magnetic field and the carrier density at D= 0.34V/nm. The range of carrier density is

chosen to lie within the one-fold degenerate phase in panel \mathbf{g} and two-fold degenerate phase in panel \mathbf{h} ; in both cases no change in the degeneracy is observed in the low- B_{l} limit.

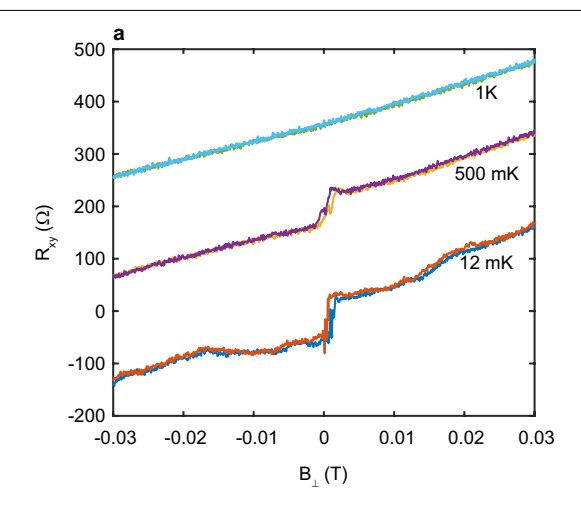


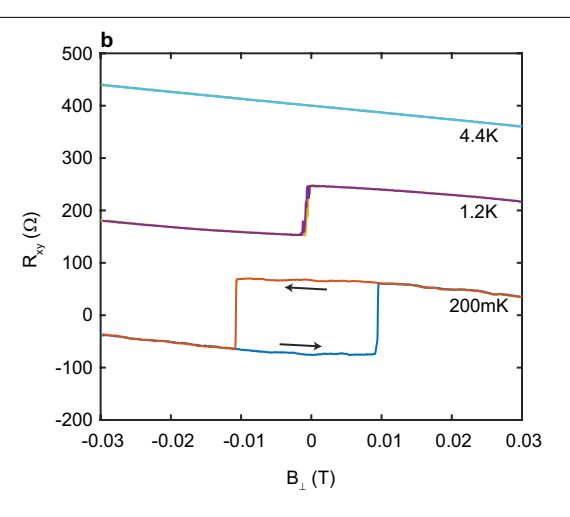




Extended Data Fig. 7 | **In-plane magnetic field dependence of the phase boundaries. a**, κ vs $n_{\rm e}$ and B_{\parallel} at D= 0.37V/nm, which covers the phase boundary between a 4-fold degenerate phase and a 1-fold degenerate phase. **b**, Same as **a**, measured at D= 0.33V/nm, which covers a phase boundary between a 1-fold

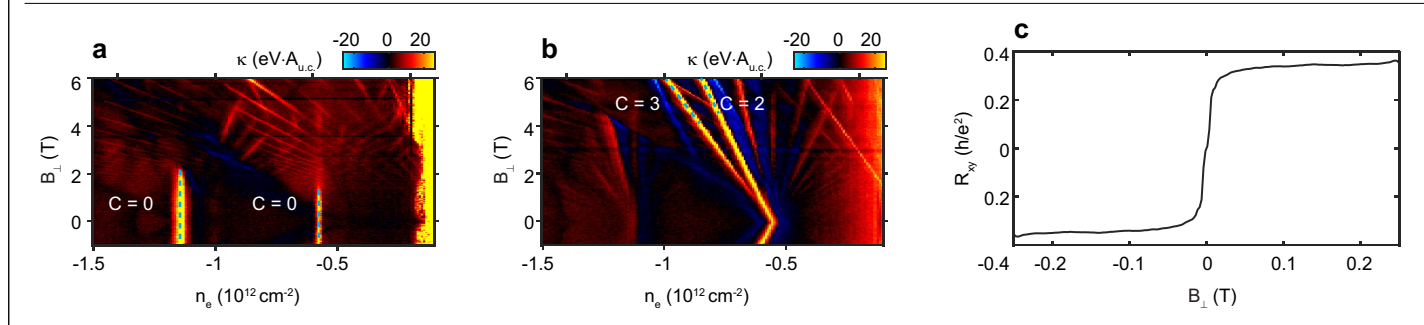
degenerate phase with a simple Fermi surface and a 1-fold degenerate phase with annular Fermi surface. \mathbf{c} , R_{xx} vs n_{e} and $B_{||}$ at D= 0.37V/nm, which covers a phase boundary between a 4-fold degenerate phase and a 2-fold degenerate phase.



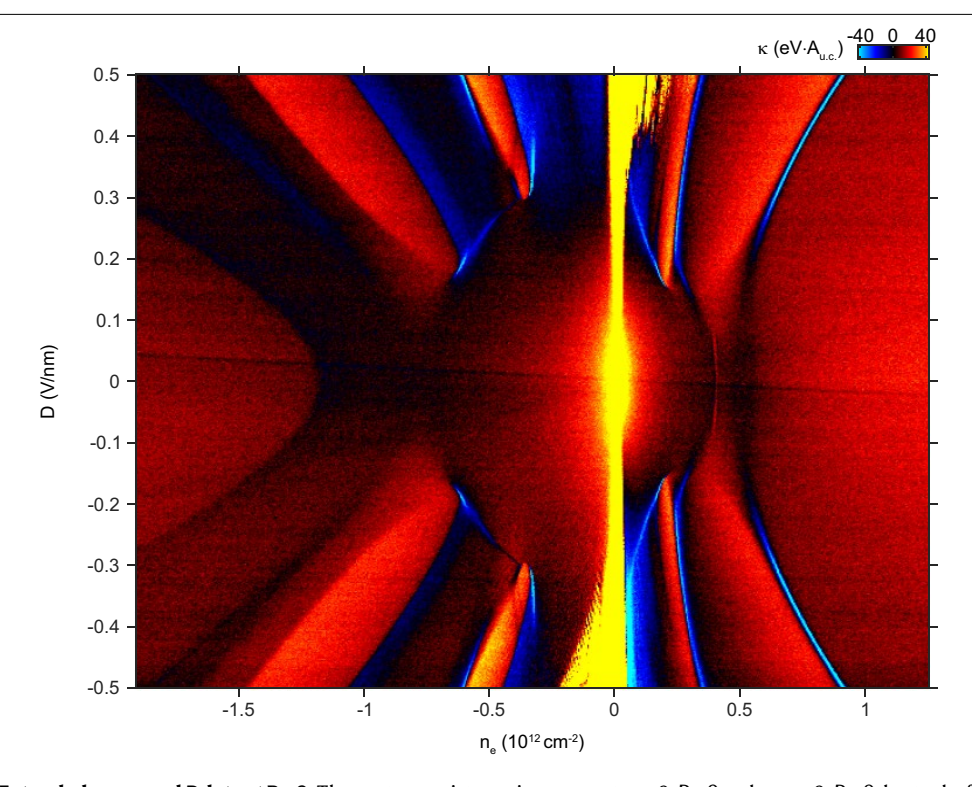


Extended Data Fig. 8 | Anomalous Hall effect and Magnetic hysteresis. a, Hall resistance R_{xy} as a function of the out-of-plane magnetic field B_{\perp} measured at $n_{\rm e}=0.19\times 10^{12}{\rm cm}^{-2}$, D=-0.4 V/nm. b, Same measurement at $n_{\rm e}=0.43\times 10^{12}{\rm cm}^{-2}$, D=0.38 V/nm with a 0.1T in-plane magnetic field applied.

The curves measured at different temperatures are offset by 200Ω for clarity. The Hall resistance was obtained by measuring the four-terminal resistance in two configurations and applying the Onsager reciprocal relation.



Extended Data Fig. 9 | **Magnetic field response of the insulating states in Sample B. a**, Inverse compressibility versus carrier density and out-of-plane magnetic field at D= 0.52V/nm measured in sample B. **b**, Same as **a**, measured at D=-0.57 V/nm. **c**, R_{xy} versus B_{\perp} measured at R_{e} = -0.52 × 10¹² cm⁻², D=-0.47 V/nm.



Extended Data Fig. 10 | **Extended K vs** n_e **and** D **data at B = 0.** The contact resistance increases at $n_e > 0$, D > 0 and at $n_e < 0$, D < 0 due to the formation of a pn-junction near the contact, producing the defect features near the charge neutrality point.